Temperature Measurements in Resistance-Heated Specimens: Longitudinal Gradients

Holes drilled in Gleeble test specimens functioned as black-body radiating cavities from which longitudinal temperature profiles could be established

BY D. W. WALSH, M. J. CIESLAK AND W. F. SAVAGE

ABSTRACT. Longitudinal temperature profiles were measured in cylindrical Gleeble specimens of Type 304 stainless steel and AISI 1018 plain carbon steel. Holes drilled into the specimen at 2.54 mm (0.1 in.) intervals acted as black-body radiating cavities. Temperature measurements were made in the holes in the range of 750° to 1100°C (1382° to 2030°F) using an optical pyrometer. Regions of essentially constant temperature were found in a variety of the samples tested. In general, longer jaw separations, higher test temperatures, smaller specimen diameters, and lower specimen thermal diffusivities favor the establishment of a constant temperature region.

Introduction

The Gleeble, a thermo-mechanical testing device, has been used in a wide range of applications involving study of a variety of materials problems. These include, but are not limited to, studies of hot ductility (Refs. 1-4), mechanical properties of the weld HAZ (Refs. 5-14), continuous cooling transformation diagrams (Refs. 15-17), stress relief cracking (Ref. 18), precipitation kinetics (Ref. 19), basic weldability studies (Refs. 20-24), strain age cracking (Refs. 25, 26), constitutional liquation (Ref. 27), liquid metal embrittlement (Refs. 28, 29), and solidification of austenitic stainless steel weldments (Refs. 30, 31).

The Gleeble 1500 system permits simulation of virtually any thermo-mechanical process. A dedicated minicomputer can be readily programmed to provide reference signals for closed loop control of both the thermal and the mechanical operations.

Heating is accomplished by the flow of low-frequency alternating current in the specimen, and heating rates up to 10,000°C (18,032°F) per second can be obtained. The feedback signal necessary for closed loop control is normally obtained from a fine wire thermocouple percussion welded to the specimen surface. However, for temperatures above the operating limits of thermocouples, a radiation pyrometer can be employed at some sacrifice in the overall response time of the system.

Though the Gleeble has a long and proven history as a tool for both the study of metallurgical phenomena at the research level and for materials testing to predict service behavior at the production level, little information on the longitudinal thermal profiles in test specimens has been published. The present work was performed to answer basic questions about the effects of specimen diameter, peak temperature, jaw separation, and material type on the thermal profiles in specimens that are subjected to similar thermal programs.

The application of optical pyrometry coupled with the drilling of black-body simulators along the specimen length allowed thermal data to be collected with a density of defined points not feasible through the employment of thermocouple technology alone. The optical pyrometer used in this research had an accuracy of 1% of the temperature measured. The calibration of the instrument was traceable to the National Bureau of Standards. The method of optical pyrometry is more precise than measurement by thermocouple because of inherent differences among welded thermocouple hot junctions. The data gathered in this study, therefore, allowed longitudinal thermal profiles in Gleeble specimens to be determined with confidence and correlations with specimen variables to be drawn.

Materials and Procedures

Two different materials were used in this study, Type 304 stainless steel and AISI 1018 carbon steel. Each was supplied as round bar stock of either 10.0 or 6.35 mm (0.4 or 0.25 in.) diameter. Samples of both diameters of each material were cut to 20.0 and 15.0 cm (7.9 and 5.9 in.) lengths and holes were drilled perpendicular to the surface at 0.254 cm (0.10 in.) intervals on a line parallel to the cylindrical axis. The first hole was drilled at the longitudinal center of the bar, and the remainder on 0.254 cm intervals throughout the free span of the specimen. A total of 33 holes were drilled in the 20 cm bars, while 15 holes were drilled in 15 cm bars. The hole diameter was 1.18 mm (0.05 in.) in the 10.0 mm diameter bars and 0.84 mm (0.03 in.) in the 6.35 mm bars. The depth of holes was such that a seven-to-one ratio was maintained between the hole depth and hole diameter. The seven-to-one aspect ratio was desired so that the holes would behave as quasi-black-body radiators.

Cavities were used to avoid problems associated with the variable emissivity of surfaces. The emissivity of a surface is a function of surface composition, geometry and temperature. The radiance of a surface is a function of this emissivity and temperature. The radiance of a cavity, however, is a function only of temperature in the ideal case, but to a close approximation, this is so even in the real case. This material independence can be visualized by postulating two abutting

Paper presented at the 63rd AWS Annual Convention, held in Kansas City, Mo., April 25-30, 1982.

D. W. WALSH, formerly a Research Fellow at Rensselaer Polytechnic Institute (RPI), Troy, N.Y., is an Associate Professor of Metallurgical Engineering at Cal Poly State University, San Luis Obispo. W. F. SAVAGE is a Professor Emeritus at RPI. M. J. CIESLAK is a Research Engineer at Sandia Laboratories, Albuquerque, N. Mex.

hollow blocks of different material with holes opposing one another on the abutting surfaces. If we impose the restriction that the materials are at the same temperature, based upon the laws of thermodynamics there can be no net energy transfer between the two blocks. Hence, the radiance of any cavity is only a function of temperature. Thus, the problems of different surface geometries, textures, and changing composition with time (oxidation) are avoided by using the cavity approach.

Specimens were tested with a Gleeble 1500 thermo-mechanical test system equipped with water-cooled aluminum jaws and copper jaw inserts. The copper jaw inserts were of the wedge type, which insured intimate contact for heat and current at the surface.

A chromel-alumel control thermocouple was attached by percussion welding each wire individually to the sample surface to form what has been called an "open circuit" thermocouple at the mid-length. This thermocouple technique was used in lieu of a cross wire welded thermocouple so that a more reproducible hot junction could be obtained. This single wire method eliminates displacement of the effective hot junction from the specimen surface by excessive flash. The samples were placed in a controlled-atmosphere chamber and centered with the jaws at the desired separation. The axes of the holes were oriented approximately 20 deg off the vertical so that the holes, as viewed with the optical pyrometer, were parallel to the specimen diameter. When the alignment was complete, the controlled-atmosphere box was evacuated to a pressure of approximately 2 Torr and backfilled with welding-grade argon. The process was repeated three times, and the chamber was then left under a slight positive pressure of argon (10 cfh, or 4.7 L/min, excess argon flow).

The specimen was heated to the temperature of interest in 10 s, and held for a period of 2 min before making measurements. Temperature readings were then taken by locating the pyrometer directly over the hole to be observed through manipulation of a goniometer head mounted on the instrument tripod. The cavities were observed through the glass top of the atmosphere chamber. All temperature readings were made in a darkened room, and each was replicated three times. To eliminate systematic error, measurements of temperature in any one hole were not taken consecutively.

Both 6.35 and 10.0 mm diameter AISI 1018 carbon steel and 304 stainless steel bars were examined. Testing was done at three peak temperatures, 900°, 1000° and 1100°C (1652°, 1832° and 2012°F), at each of three jaw separations, 2.5, 6.35 and 11.5 cm (1, 2.5 and 4.5 in.), the

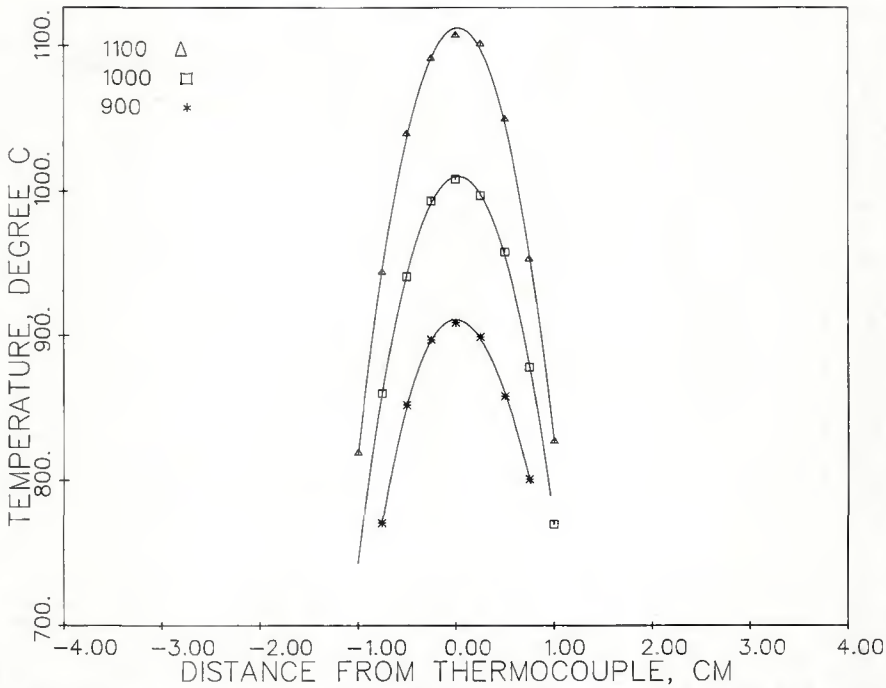

Fig. 1 — Thermal profiles in a 1.0 cm diameter 304 SS bar at a jaw separation of 2.54 cm, for peak temperatures of 900°, 1000°, and 1100°C. The symbols indicate actual experimental values; the drawn curves are least-square fits

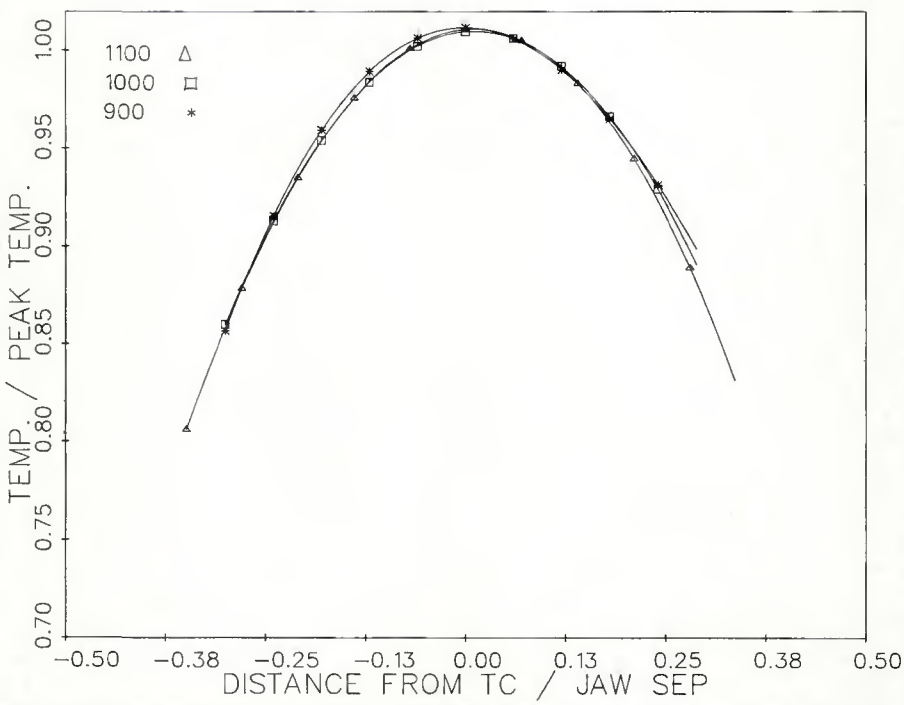

Fig. 2 — Thermal profiles in a 1.0 cm diameter 304 SS bar at a jaw separation of 2.54 cm, for peak temperatures of 900°, 1000°, and 1100°C. The data are presented in a nondimensional form. The symbols indicate actual experimental values; the curves are least-square fits

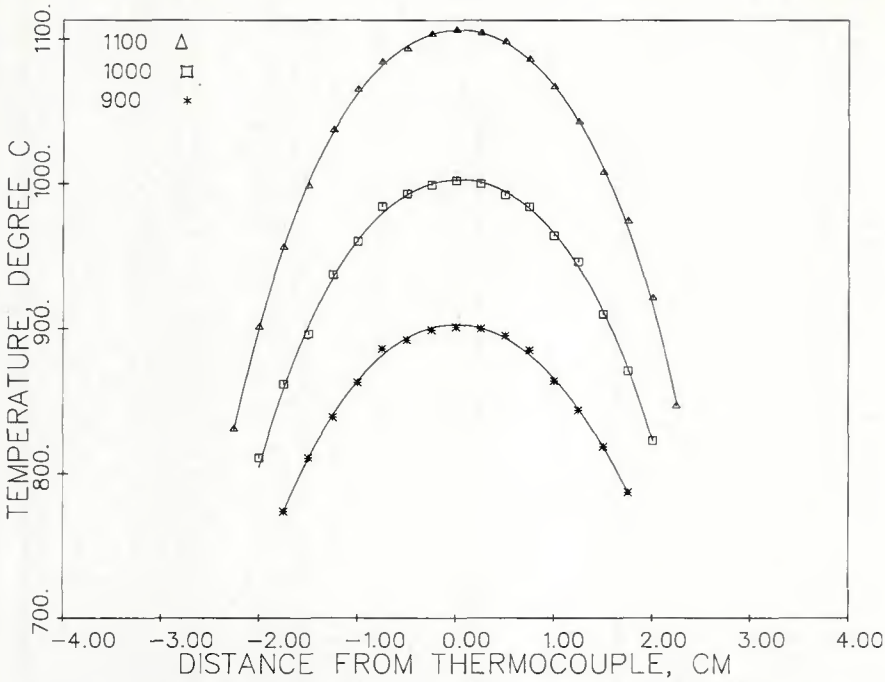

Fig. 3 — Thermal profiles in a 1.0 cm diameter 304 SS bar at a jaw separation of 6.35 cm, for peak temperatures of 900°, 1000°, and 1100°C. The symbols indicate actual experimental values; the drawn curves are least-square fits

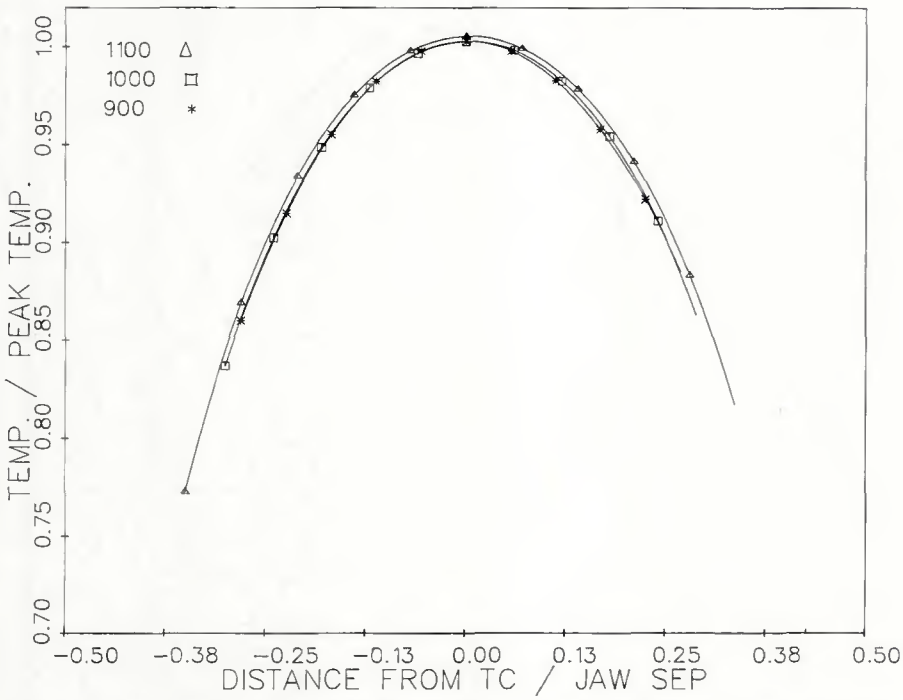

Fig. 4 — Thermal profiles in a 1.0 cm diameter 304 SS bar at a jaw separation of 2.54 cm, for peak temperatures of 900°, 1000°, and 1100°C. The symbols indicate actual experimental values; the drawn curves are least-square fits

latter being the maximum possible in the controlled-atmosphere chamber.

Results and Discussion

The data gathered are presented in two ways: in absolute readings of temperature as a function of distance from the central thermocouple, and in nondimensional form, as the ratio of temperature divided by the peak temperature versus the ratio of distance from the central thermocouple to jaw separation. Figures 1–12 depict selected data typical of the results obtained.

We may consider the sample as a system in dynamic thermal equilibrium with its surroundings. Thus, to maintain any given temperature profile, heat is supplied by the electrical current passing through the specimen, and heat is lost by three mechanisms. The first is conduction along the specimen itself, in which the heat is transferred to the water-cooled jaws. The rate of this heat flow is directly proportional to both the thermal gradient and the thermal diffusivity of the material. The second mechanism is convection in the gaseous atmosphere, which removes heat and dissipates it to the surroundings by mixing. The third is in the form of radiation emitted by the specimen. The amount of heat lost through this mode is proportional to the fourth power of the absolute temperature, and therefore becomes more important at high temperatures. Thus, the thermal profile generated by a given peak temperature, jaw separation, specimen diameter and material type is determined by a complex interplay of these mechanisms in establishing a thermal balance.

The Gleeble specimen may be treated as a uniform cylindrical bar with internal generation of heat. If convection and radiation losses are neglected, the principle of the conservation of energy leads to the following relationship for the instantaneous temperature distribution in the bar:

$$\frac{\partial T}{\partial t} = \frac{K}{\rho C_p} \nabla^2 T + \frac{I^2}{\rho C_p w^2 \sigma} \qquad (1)$$

K = Thermal conductivity
T = Temperature
ρ = Density
C_p = Heat capacity
t = Time
w = Cross-sectional area
σ = Electrical conductivity
I = Current

If we simplify the system by limiting the heat flow to one dimension, Equation 1 becomes:

$$\frac{\partial T}{\partial t} = \frac{K}{\rho C_p} \frac{\partial^2 T}{\partial x^2} + \frac{I^2}{\rho C_p w^2 \sigma} \qquad (2)$$

This relationship closely approximates the behavior of a resistance-heated specimen. If the temperature distribution within the bar is assumed to be steady state, Equation 2 reduces to the Poisson relation below:

$$\frac{\partial^2 T}{\partial x^2} = \frac{-I^2}{Kw^2\sigma} \qquad (3)$$

Therefore, if radiation and convection losses are ignored, the temperature distribution in the bar will be a parabolic one. This can be demonstrated by double integration of Equation 3 to obtain:

$$T_{(x)} = \frac{-I^2}{Kw^2\sigma} x^2 + c'x + c'' \qquad (4)$$

The constants of c' and c'' can be determined for specific boundary conditions. Solutions to this equation exist in the literature (Ref. 32) and have been applied to the determination of the lengths over which the temperature of the bar lies, between the maximum and some arbitrary lower temperature. This length is given by the following:

$$L = L_0 \left(\frac{\Delta T}{T_{max} - T_0} \right)^{1/2} \qquad (5)$$

L_0 = Jaw separation
T_0 = Temperature at the jaw
ΔT = Temperature difference

However, problems exist for this simplified treatment, since experimental results do not fit the model well. Several factors contribute to this. The thermal conductivity, k, is not a constant, and being itself a function of temperature can be presented as:

$$K = K_0 (1 - bT) \qquad (6)$$

However, since the value of b is small, an average value of k can be used over a small range of temperatures without generating an excessively large error.

The mathematics of the system become more complex when treatments for either convection or radiation heat transfer are included. Heat loss by either mechanism will tend to flatten the parabolic profile predicted by Equation 4. Convection losses can be represented by adding a single term to the Poisson equation to obtain:

$$\frac{K}{\rho C_p} \frac{\partial^2 T}{\partial x^2} + \frac{I^2}{\rho C_p w^2 \sigma}$$

$$- \frac{h\gamma}{\rho C_p w} (T - T_0) = 0 \qquad (7)$$

h = Convective heat transfer coefficient
γ = Geometry = dependent constant

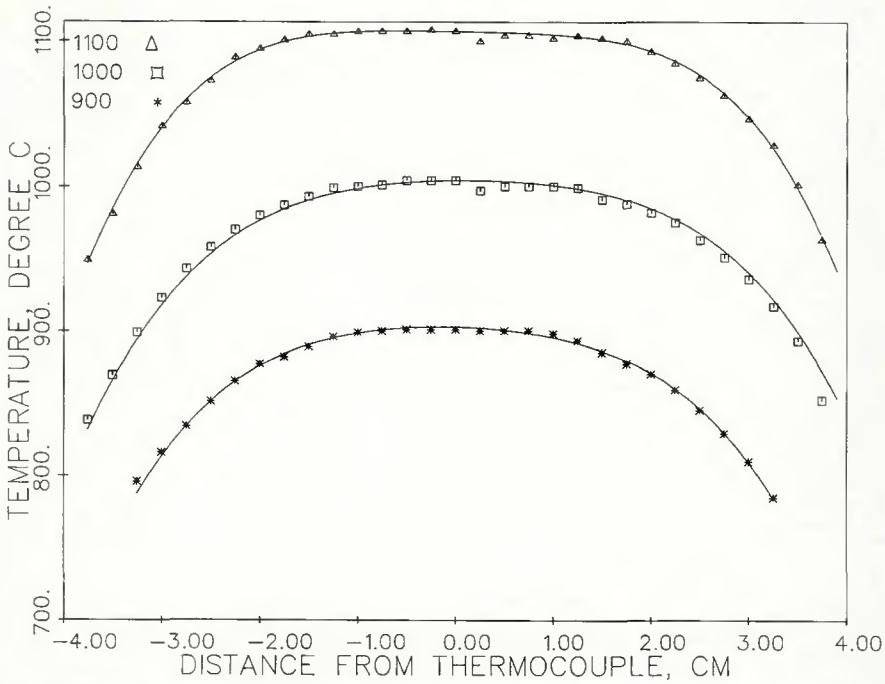

Fig. 5 — Thermal profiles in a 1.0 cm diameter 304 SS bar at a jaw separation of 11.5 cm, for peak temperatures of 900°, 1000°, and 1100°C. The symbols indicate actual experimental values; the drawn curves are least-square fits

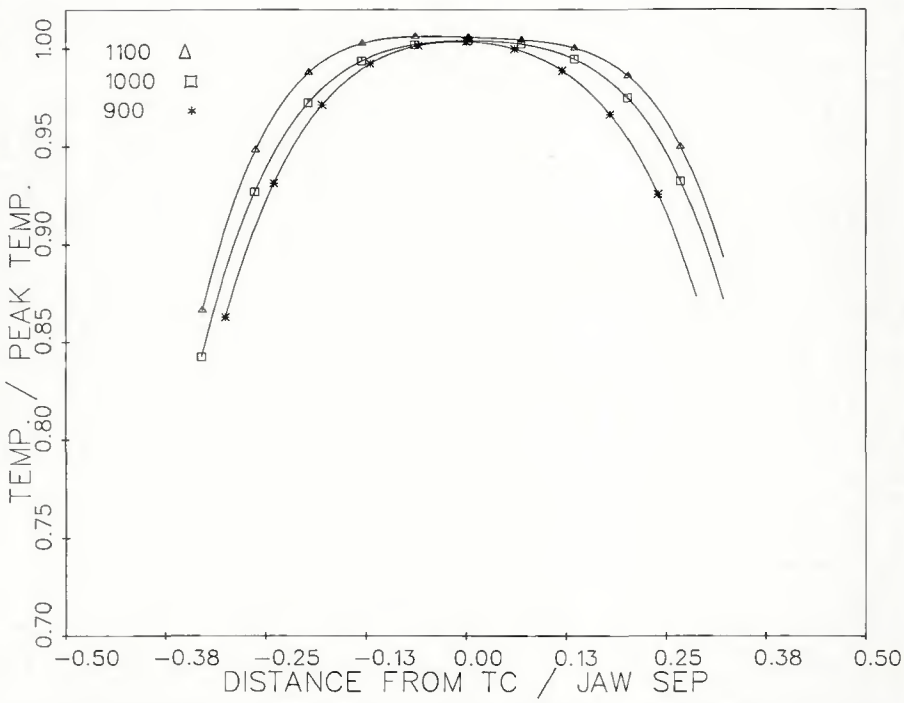

Fig. 6 — Thermal profiles in a 1.0 cm diameter 304 SS bar at a jaw separation of 11.5 cm, for peak temperatures of 900°, 1000°, and 1100°C. The data are presented in a nondimensional form. The symbols indicate actual experimental values; the curves are least-square fits

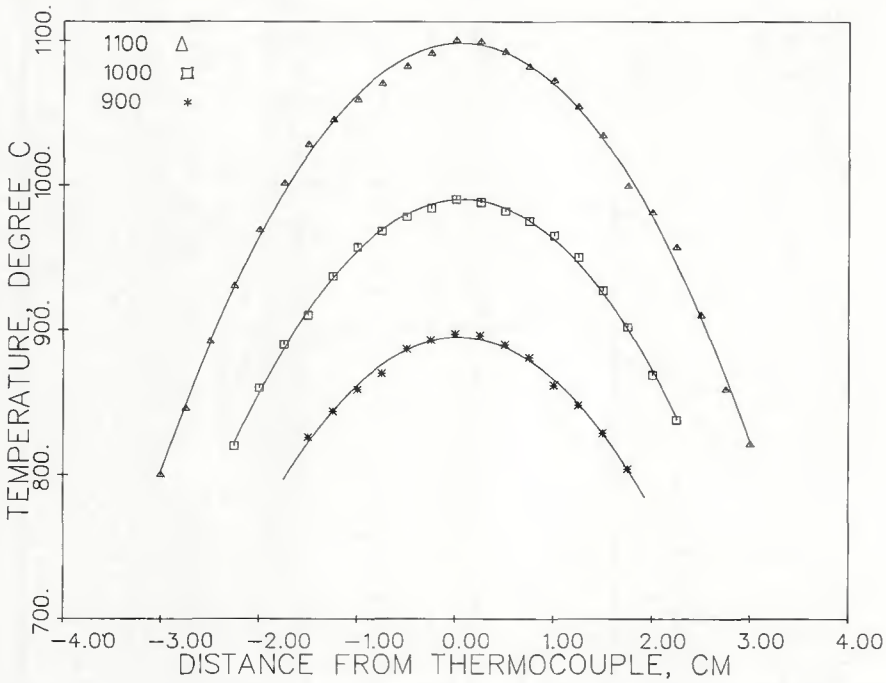

Fig. 7 — Thermal profiles in a 1.0 cm diameter AISI 1018 CS bar at a jaw separation of 11.5 cm, for peak temperatures of 900°, 1000°, and 1100°C. The symbols indicate actual experimental values; the drawn curves are least-square fits

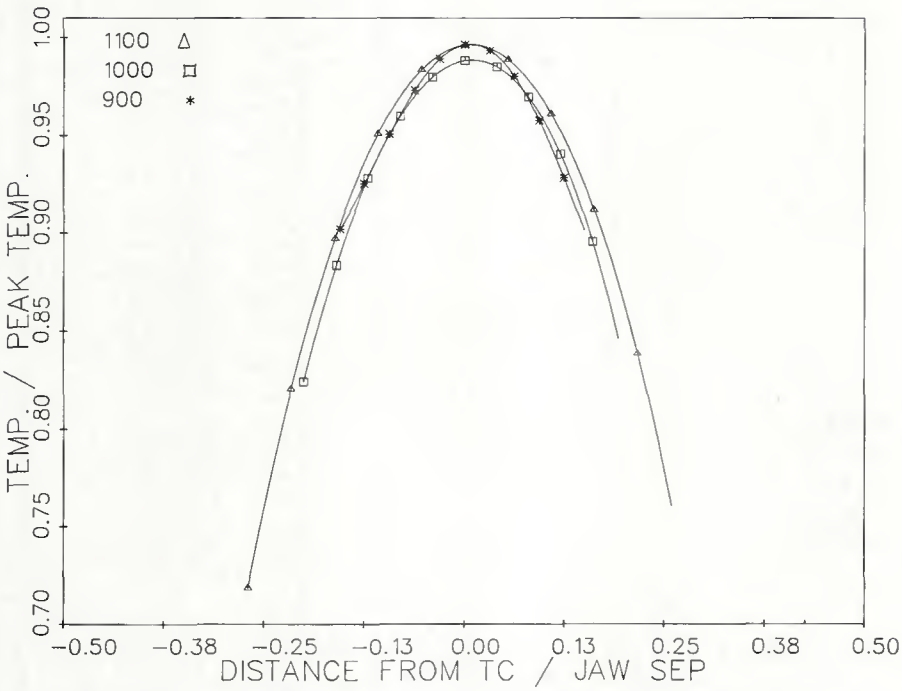

Fig. 8 — Thermal profiles in a 1.0 cm diameter AISI 1018 CS bar at a jaw separation of 11.5 cm, for peak temperatures of 900°, 1000°, and 1100°C. The data are presented in a nondimensional form. The symbols indicate actual experimental values; the curves are least-square fits

The inclusion of another temperature-dependent term makes the solution to the differential equation more complex, and leads to solutions involving hyperbolic functions. The addition of a term for radiation losses further complicates the solution, since the radiative heat loss, Q_{12}, is proportional to the fourth power of absolute temperature, as shown below:

$$Q_{12} = F_{12}\alpha(T_1^4 - T_2^4) \qquad (8)$$

Q_{12} = Heat transfer from Body 1 to Body 2
F_{12} = View factor, Body 1 to Body 2
T_i = Temperature of Body 1
α = The Stephan-Boltzman constant

The constants h, in the convective solution, and α, in the radiative solution, are small, and high temperatures are required before convection and radiation play a major role in determining the temperature profile in the bar.

Figure 1 presents the unnormalized data collected for a 10.0 mm (0.4 in.) stainless steel bar, a jaw separation of 2.54 cm (1 in.), and peak centerline temperatures of 1100°, 1000° and 900°C (2012°, 1832° and 1652°F). The symbols on the plots are actual data points, while the curves are fourth-order polynomial least-square fits. Note that these plots are parabolic in appearance, and have the same general form for all three peak temperatures. Since the bar can be considered to be in dynamic thermal equilibrium, this suggests that similar modes of heat flow are involved at all three temperatures. This conclusion is supported by Fig. 2, where the data used to generate Fig. 1 are converted to a nondimensional form. The abscissa is the distance from the specimen center divided by the jaw separation, and the ordinate is the temperature at the particular location divided by the programmed temperature. Note that the curves appear to be superimposed in this figure. At this short jaw separation of 2.54 cm, the conduction of heat to the jaws is the primary mode of heat loss from the bar, with convection and radiation losses being insignificant. Thus, the parabolic shape is exactly as predicted by Equation 4. However, Equation 5 fails to predict the zone length, L, because changing the peak temperature alters the effective values of both L_0 and T_0. The lack of agreement with experimental data becomes even greater under conditions where convection and radiation losses are significant.

Figure 3 shows data for a 10.0 mm stainless steel bar over the same temperature range with a 6.35 cm (2.5 in.) jaw separation. Each of the curves generated is again roughly parabolic and of the

same general form. Again this implies that the thermal processes are similar for the two jaw separations and that conduction is the dominant process. For a given peak temperature, the curve in Fig. 3 has a lesser slope than its counterpart in Fig. 1. This results from the fact that the heat must diffuse a greater distance with the longer jaw separation before it reaches the heat sink. Figure 4 is the nondimensional representation of the data shown in Fig. 3. Again the three curves superimpose within the experimental error, thus supporting the contention that conduction is the primary mechanism of heat loss in 10.0 mm diameter stainless steel bars at both 2.54 and 6.35 cm jaw separations. Furthermore, the curves of Fig. 4 can be superimposed directly upon those of Fig. 2, despite the large difference in the jaw separations involved. This provides an even stronger indication that the same physical phenomena control heat loss in both cases.

Figure 5 presents data for a 10.0 mm stainless steel bar with an 11.5 cm (4.5 in.) jaw separation. In this case, a zone of relatively constant temperature developed, and the family of curves is no longer parabolic. Thus, it appears that confounding terms have entered the expression for temperature as a function of distance from the thermocouple. Conduction no longer completely dominates the thermal equilibrium of the bar, and both radiation and/or convection must now play significant roles in heat loss. This is especially true over the central regions where shallow thermal gradients exist. Therefore, it appears that at higher temperatures the heretofore primary mechanism, heat loss by conduction through the bar to the jaws, is no longer the overwhelmingly dominant mechanism of heat extraction.

With the 11.5 cm jaw separation, three factors appear to be important. First, the longer free span between the jaws requires the generation of more heat in order to produce a steady-state condition with a given peak temperature. Second, the heat-flow path length is nearly doubled over the 6.35 cm jaw separation, and third, the ability of the jaws to conduct away the greater amount of heat is exceeded.

The nondimensional data, shown in Fig. 6, also supports the conclusion that a major change in the mechanism of heat loss has occurred. These plots, unlike the previous nondimensional plots, are no longer parabolic. The change is caused by the increase in the separation of the jaws, and the extent of the disparity appears to be greater at higher peak temperatures. This implies that the increase in both the total heat generated and the length of the heat-flow path are critical factors which reduce the domi-

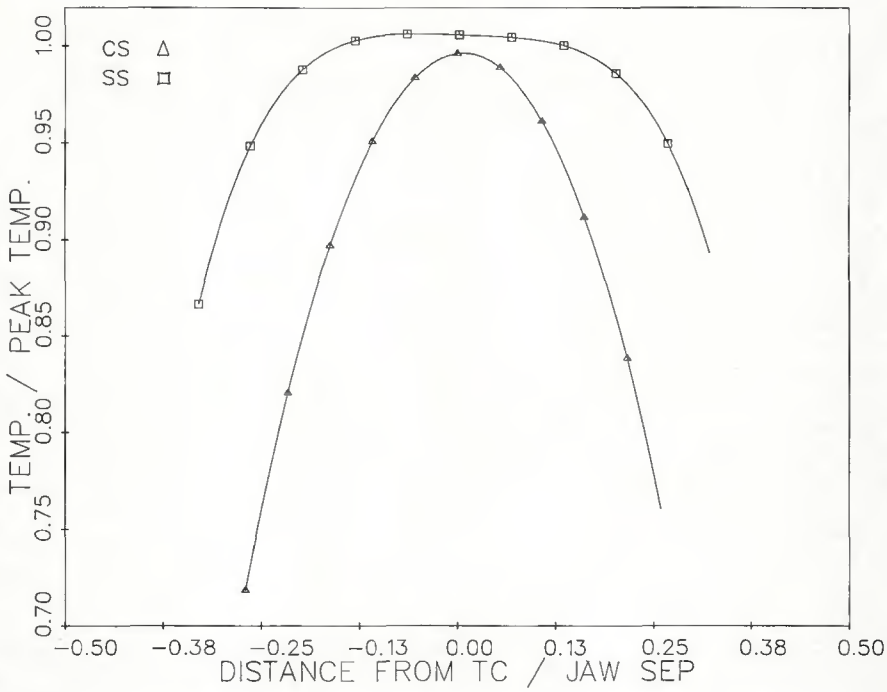

Fig. 9 — Thermal profiles in 1.0 cm diameter 304 SS and AISI 1018 CS bars at a jaw separation of 11.5 cm, for a peak temperature of 1100°C. The data are presented in a nondimensional form. The symbols indicate actual experimental values; the curves are least-square fits

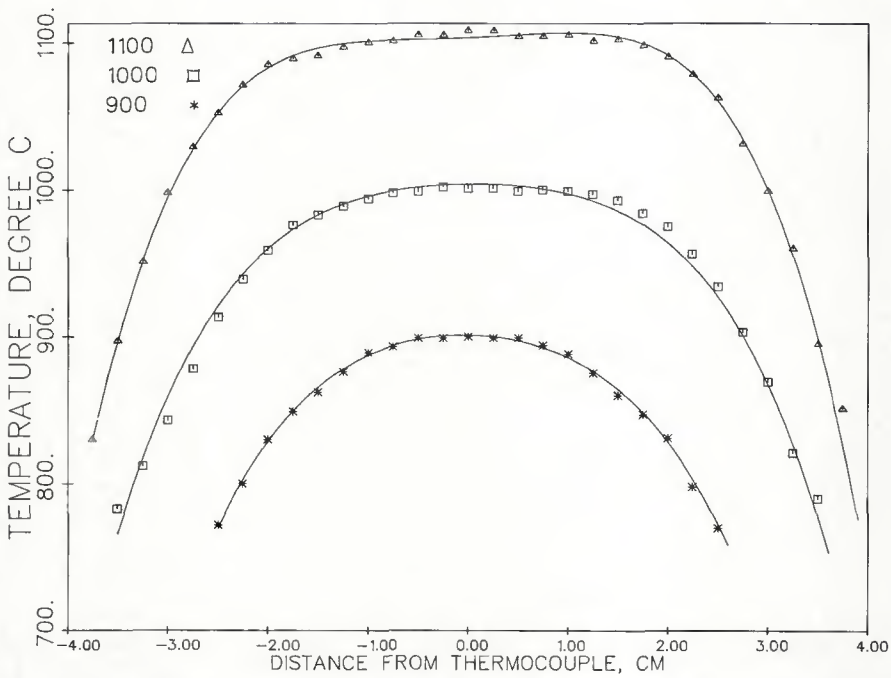

Fig. 10 — Thermal profiles in a 0.635 cm diameter AISI 1018 CS bar at a jaw separation of 11.5 cm, for peak temperatures of 900°, 1000°, and 1100°C. The symbols indicate actual experimental values; the drawn curves are least-square fits

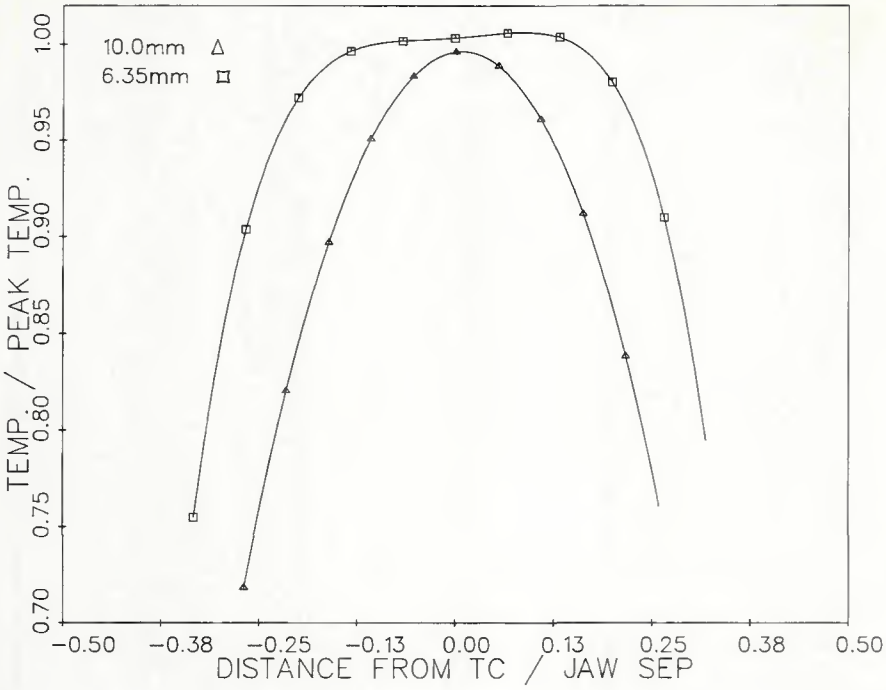

Fig. 11 — Thermal profiles in both 1.0 cm and 0.635 cm AISI 1018 CS bars at a jaw separation of 11.5 cm, for a peak temperature of 1100°C. The data are presented in a nondimensional form. The symbols indicate actual experimental values; the curves are least-square fits

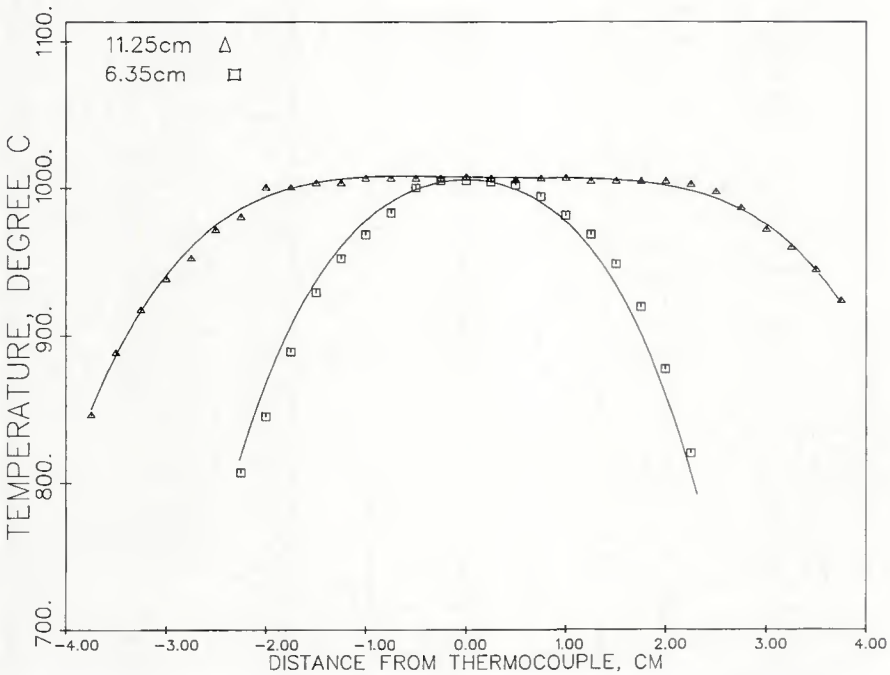

Fig. 12 — Thermal profiles in a 0.635 cm diameter 304 SS bar at jaw separations of 11.5 and 6.35 cm, for a peak temperature of 1000°C. The symbols indicate actual experimental values; the drawn curves are least-square fits

nance of conductive heat loss with an 11.5 cm jaw separation.

In Fig. 7, data are presented for 10 mm diameter AISI 1018 plain carbon steel specimens with an 11.5 cm jaw separation for peak temperatures of 1100°, 1000°, and 900°C, a combination of variables equivalent to that for the stainless steel bar discussed above in connection with Fig. 5. Under these conditions, the carbon steel bars generate thermal profiles that are approximately parabolic in every case. The parabolic nature is also evident in the nondimensional plots shown in Fig. 8. In the case of 10 mm carbon steel bars, the heat flow mechanism is not conduction limited. This is not surprising, since the thermal diffusivity of carbon steel is much greater than that of stainless steel. However, if we compare the thermal profiles for carbon steel in Fig. 8 with Figs. 2 and 4, the conduction-dominated cases for stainless steel, we note that the slopes are steeper for the carbon steel. This difference is a direct result of the higher thermal diffusivity of the carbon steel. The effect of this difference in thermal diffusivity is emphasized in Fig. 9, where the nondimensional plots for 10 mm bars of both carbon steel and stainless steel are juxtaposed for a peak temperature of 1100°C with an 11.5 cm jaw separation. The approximately parabolic shape of the carbon steel profile persists because of the dominance of the conduction mechanism, whereas the Type 304 stainless steel, with its markedly lower thermal conductivity, develops a central region with only a minute longitudinal thermal gradient. Thus, the stainless bar simply cannot lose heat by conduction as readily as can the carbon steel bar.

Figure 10 shows the thermal profiles generated at peak temperatures of 1100°, 1000°, and 900°C in a 6.35 mm carbon steel bar for a jaw separation of 11.5 cm. In every case, the thermal profiles deviated from the simple parabolic shapes produced in the 10.0 mm carbon steel bar under the same conditions. Note also that in Fig. 10 the length of the low gradient region increases as the peak temperature increases.

The effect of diameter can be seen directly in Fig. 11. This figure compares nondimensional plots of the thermal profiles in carbon steel bars with a peak temperature of 1100°C for bar diameters of both 10.0 and 6.35 mm and a jaw separation of 11.5 cm. Note that the 10.0 mm bar exhibits no deviation from the parabolic form, indicating that conduction is the dominant mode of heat loss. However, the 6.35 mm bar exhibits an extensive region of shallow thermal gradient, indicating that the heat-flow process is a combination of all three phenomena. Thus, the extremely small tem-

Table 1—Equations for Thermal Distribution—Nondimensional Fit

Material	Diameter (cm)	Jaw Separation (cm)	T (°C)	a	b	c	d	e
CS	1.0	11.45	1100	−3.878	−0.179	−3.392	0.498	0.996
CS	1.0	11.45	1000	−10.322	−1.271	−3.592	0.070	0.988
CS	1.0	11.45	900	50.565	−3.993	−5.278	0.072	0.996
CS	1.0	6.35	1100	0.540	−0.105	−2.732	−0.076	0.998
CS	1.0	6.35	1000	0.763	−0.244	−2.698	−0.036	1.001
CS	1.0	6.35	900	18.337	0.597	−3.587	−0.066	0.999
CS	1.0	2.54	1100	6.500	−0.774	−2.980	0.153	0.987
CS	1.0	2.54	1000	9.924	−0.722	−3.211	0.132	0.989
CS	1.0	2.54	900	18.518	−2.140	−3.836	0.196	0.989
CS	0.635	11.45	1100	−22.254	−0.365	0.106	0.033	1.003
CS	0.635	11.45	1000	−20.239	−0.239	−0.567	0.042	1.003
CS	0.635	11.45	900	−22.523	0.139	−1.903	−0.009	1.002
CS	0.635	6.35	1100	−1.651	−0.325	−3.580	0.091	1.006
CS	0.635	6.35	1000	−1.480	0.346	−3.540	0.077	1.003
CS	0.635	6.35	900	−13.152	0.459	−3.145	0.082	1.002
CS	0.635	2.54	1100	1.240	−0.051	−2.645	0.065	1.008
CS	0.635	2.54	1000	5.00	0.444	−3.042	0.089	1.008
CS	0.635	2.54	900	−1.388	0.093	−2.708	0.093	1.005
SS	1.0	11.45	1100	−10.627	0.339	−0.052	−0.014	1.008
SS	1.0	11.45	1000	−9.167	0.204	−0.407	0.004	1.004
SS	1.0	11.45	900	−9.058	0.069	−0.783	−0.016	1.004
SS	1.0	6.35	1100	−3.338	0.232	−1.391	0.007	1.005
SS	1.0	6.35	1000	−3.323	0.071	−1.481	0.014	1.003
SS	1.0	6.35	900	−1.791	0.342	−1.594	−0.001	1.003
SS	1.0	2.54	1100	−0.283	−0.131	−1.601	0.029	1.011
SS	1.0	2.54	1000	−0.426	−0.008	−1.514	0.034	1.010
SS	1.0	2.54	900	−0.168	0.679	−1.523	−0.006	1.012
SS	0.635	11.45	1100	−9.815	0.974	0.291	−0.025	1.005
SS	0.635	11.45	1000	−9.951	0.993	−0.005	0.001	1.008
SS	0.635	11.45	900	−9.239	0.623	−0.246	0.033	1.000
SS	0.635	6.35	1100	−5.823	−0.073	−0.667	−0.033	1.004
SS	0.635	6.35	1000	−2.504	−0.079	−1.159	0.039	1.002
SS	0.635	6.35	900	−1.733	−0.072	−1.334	0.045	1.009

$T/T_{peak} = ax^4 + bx^3 + cx^2 + dx + e$
x = distance from CL/jaw separation

perature gradients created near the center of the 6.35 mm bar decrease the amount of heat flow by conduction to the point where convection and radiation become the dominant factors controlling the heat loss with the larger jaw separations. Hence, the low gradient zone grows longer. Slimmer rods, because of the greater surface-to-volume ratio, will be impacted by convection and radiation at lower peak temperatures and shorter jaw separations.

Figure 12 gives direct evidence of the effects of jaw separation. Data are shown for a 6.35 mm diameter stainless steel bar, a peak temperature of 1000°C and jaw separations of 11.5 and 6.35 cm. Note that the smaller jaw separation both diminishes the heat content of the bar for a given peak temperature and decreases the distance heat must flow to reach the water-cooled copper jaws. Furthermore, since with the smaller jaw separation a steeper thermal gradient is present, the effective thermal conductivity of the bar is higher, because a larger fraction of the heat-flow path is at a lower temperature, where the thermal conductivity is greater. Thus, at short jaw separation, radiation and convection would become significant only at very high temperatures or in materials with low thermal conductivities. Longer jaw separations promote the creation of a low gradient in the central region, as a result of conduction-delimited heat flow.

Table 1 lists the coefficients generated by a fourth-order least-squares polynomial fit to the temperature profile data for the nondimensional representations. The gradient at any point can be found by using the derivative of these equations with respect to x, and substituting the appropriate nondimensional distance. Furthermore, the span over which the temperature of the bar lies, between the maximum temperature and any chosen lower temperature, can be found by substituting the nondimensional temperature into the expressions and solving for x.

Conclusions

1. Optical pyrometry can be used to measure the temperature of Gleeble specimens if suitable radiant cavities are created.

2. Higher peak temperature, smaller bar diameters, greater jaw separations and lower thermal diffusivities all decrease the thermal gradients in the specimens and promote the formation of a central region of nearly constant temperature.

3. Polynomial equations have been developed that describe the thermal profiles which exist in test samples under a wide variety of operator-controlled conditions.

4. At a particular peak temperature, a span in which the temperature lies within a desired percentage of the peak temperature can be generated by a judicious choice of operating conditions and specimen geometries.

5. Any operation that diminishes the thermal conductivity at the jaw will promote the generation of a region in the specimen with a minute longitudinal thermal gradient.

6. The generation of a region of minute thermal gradient in a specimen inhibits rapid, dynamic thermal work since the cooling rate is proportional to the longitudinal thermal gradient.

References

1. Nippes, E.F., Savage, W.F., Bastian, B.J., and Curran, R.M. 1955. An investigation of the

hot ductility of high-temperature alloys. *Welding Journal* 34(4):183-s to 196-s.

2. Nippes, E.F., Savage, W.F., and Grotke, G. 1957. Further studies of the hot ductility of high-temperature alloys. *Welding Research Council Bulletin Series* 33(2):32.

3. Kreischer, C.H. 1963. A critical analysis of the weld heat-affected zone hot ductility test. *Welding Journal* 42(2):49-s to 59-s.

4. Weiss, B., Grotke, B.E., and Stickler, R. 1970. Physical metallurgy of hot ductility testing. *Welding Journal* 49(10):471-s to 487-s.

5. Nippes, E.F., Savage, W.F., and Paez, J.M. 1960. Impact characteristics of heat-affected zones in Mn-Mo armor steels. *Welding Journal* 39(1):31-s to 39-s.

6. Wu, K.C. 1963. A study of the weld heat-affected zone of centrifugally cast 5% chromium steel. *Welding Journal* 42(9):392-s to 396-s.

7. Nippes, E.F., and Emmerich, E.W. 1963. Heat-affected zone study of an eutectoid ultra-high strength steel. *Welding Journal* 42(12):547-s to 556-s.

8. Peterson, W.A. 1964. Weld heat-affected zone of 18% nickel maraging steel. *Welding Journal* 43(9):428-s to 432-s.

9. Savage, W.F., and Krantz, B.M. 1966. An investigation of hot cracking in Hastelloy X. *Welding Journal* 45(1):13-s to 25-s.

10. Owczarski, W.A., Duval, D.S., and Sullivan, C.P. 1966. A model for heat-affected zone cracking in nickel-base superalloys. *Welding Journal* 45(4):145-s to 155-s.

11. Connor, L.P., Rathbone, A.M., and Gross, J.H. 1967. Effects of composition on the heat-affected zone toughness of constructional alloy steels. *Welding Journal* 46(5):217-s to 234-s.

12. Mueller, R.A., Howden, D.G., and Simmons, F.B. 1973. HAZ thermocycle and structure simulation. *Welding Journal* 52(10):411-s to 416-s.

13. Hannery, N.E. 1975. Effect of Cb on HAZ ductility in constructional HT steels. *Welding Journal* 54(5):162-s to 168-s.

14. Matthews, S.J. 1979. Simulated heat-affected zone studies of Hastelloy alloy B-2. *Welding Journal* 58(3):91-s to 95-s.

15. Fastini, R.F., and Semchyshen, M. Sept. 1964. The effect of molybdenum on the continuous cooling transformation of a 0.40% carbon steel. *AMS Transactions Quarterly.*

16. Howden, D.G. 1967. Isothermal transformation characteristics of a low-alloy steel using a weld thermal cycle simulator. *Canadian Metallurgical Quarterly* 6(3).

17. Wu, K.C. 1968. Continuous-cooling transformation diagrams of Ti-8Al-1Mo-1V, *Trans. ASM* 61:621-626.

18. Meitzner, C.F., and Pense, A.W. 1969. Stress-relief cracking in low-alloy steel weldments. *Welding Journal* 48(10):431-s to 440-s.

19. Dix, A.W., and Savage, W.F. 1973. Short time aging characteristics of Inconel X-750. *Welding Journal* 52(3):135-s to 144-s.

20. Matthews, S.J. 1968. Weldability observations in 70/30 copper-nickel tubesheet material. *Welding Journal* 47(4):155-s to 161-s.

21. Wu, K.C., and Krinke, T.A. 1968. Weldability studies for AFC-77 — part 1: mechanical properties. *Welding Journal* 47(6):332-s to 336-s.

22. Peterson, W.A. 1969. Weldability of a chromium strengthened copper-nickel alloy. *Welding Journal* 48(10):425-s to 430-s.

23. Gordine, J. 1977. The weldability of some ARtic-grade line-pipe steels. *Welding Journal* 56(7):201-s to 210-s.

24. Savage, W.F., Nippes, E.F., and Casteras, J.E. 1978. Effect of alloying additions on the weldability of 70 Cu-30 Ni. *Welding Journal* 57(12):375-s to 382-s.

25. Hughes, W.P., and Berry, T.F. 1967. A study of the strain-age cracking characteristics in welded Rene 41 — phase I. *Welding Journal* 46(8):361-s to 370-s.

26. Dix, A.W., and Savage, W.F. 1971. Factors influencing strain-age cracking in Inconel X-750. *Welding Journal* 50(6):247-s to 252-s.

27. Pepe, J.J., and Savage, W.F. 1967. Effects of constitutional liquation in 18-Ni maraging steel weldments. *Welding Journal* 46(9):411-s to 422-s.

28. Savage, W.F., Nippes, E.F., and Mushala, M.C. 1978. Copper-contamination cracking in the weld heat-affected zone. *Welding Journal* 57(5):237-s to 245-s.

29. Savage, W.F., Nippes, E.F., and Mushala, M.C. 1978. Liquid-metal embrittlement of the heat-affected zone by copper contamination. *Welding Journal* 57(8):237-s to 245-s.

30. Lippold, J.C., and Savage, W.F. 1979. Solidification of austenitic stainless steel weldments: part 1 — a proposed mechanism. *Welding Journal* 58(12):362-s to 374-s.

31. Lippold, J.C., and Savage, W.F. 1980. Solidification of austenitic stainless steel weldments: part 2 — the effect of alloy composition on ferrite morphology. *Welding Journal* 59(2):48-s to 58-s.

32. Widgery, D.J. April 1972. The design and use of resistance heated weld thermal simulators. *Proceedings of the Conference on Weld Thermal Simulators for Research and Problem Solving,* The Welding Institute, Cambridge, England.

33. Welty, J.R., Wicks, C.E., and Wilson, R.E. 1969. *Fundamentals of Momentum, Heat and Mass Transfer,* 1st edition, John Wiley and Sons, Publishers.

WRC Bulletin 312
February 1986

Joining of Molybdenum Base Metals and Factors which Influence Ductility
By A. J. Bryhan

This report discusses the current status of the joining technology of molybdenum-based metals and alloys. Information of practical significance is included, which will assist in both the design and utilization of molybdenum-based metals.

Publication of this report was sponsored by the AMAX Metals Group—Research Laboratory and the Reactive and Refractory Metals Committee of the Welding Research Council. The price of WRC Bulletin 312 is $14.00 per copy, plus $5.00 for postage and handling. Orders should be sent with payment to the Welding Research Council, Ste. 1301, 345 E. 47th St., New York, NY 10017.